INTERNATIONAL JOURNAL FOR NUMERICAL METHODS IN FLUIDS
Int. J. Numer. Meth. Fluids 2000; **33**: 609–626

Numerical simulation of confined laminar jet flows

A.S.R. Sarma[a], T. Sundararajan[a,*] and V. Ramjee[b]

[a] *Department of Mechanical Engineering, Indian Institute of Technology, Madras 600 036, India*
[b] *Department of Applied Mechanics, Indian Institute of Technology, Madras 600 036, India*

SUMMARY

Two-dimensional incompressible jet development inside a duct has been studied in the laminar flow regime, for cases with and without entrainment of ambient fluid. Results have been obtained for the flow structure and critical Reynolds number values for steady asymmetric jet development and for the onset of temporal oscillations, at various values of the duct-to-jet width ratio (aspect ratio). It is found that at low aspect ratios and Reynolds numbers, jet development inside the duct is symmetric. For larger aspect ratios and Reynolds numbers, the jet flow at steady state becomes asymmetric with respect to the midplane, and for still higher values, it becomes oscillatory with respect to time. When entrainment is present, the instabilities of asymmetric development and temporal oscillations occur at a much higher critical Reynolds number for a given aspect ratio, indicating that the stability of the jet flow is higher with entrainment. Copyright © 2000 John Wiley & Sons, Ltd.

KEY WORDS: bifurcation; confinement; entrainment; instability; jets

1. INTRODUCTION

Jet flows are encountered in a wide variety of applications, such as gas turbine combustors, industrial burners, ejector systems, rocket nozzles, etc. From the fundamental point of view, jets exhibit a wide range of intriguing flow features, such as oscillatory instabilities, asymmetric development inside confined spaces, entrainment and mixing with ambient fluid, etc. In the present work, the flow features and entrainment characteristics of confined laminar jets are investigated. Analytical solutions for free jet flows are available, based on the self similarity of velocity field [1]. However, these solutions are valid only far away from the jet inlet, and in most applications, the near-field development holds the key to important features of the jet flow. Therefore, the near-field development of a jet has been the subject of a lot of research in recent years.

The flow features of confined laminar jets can be analysed from two view points. For large aspect ratios (duct width/jet width), the flow development of a confined jet is akin to that of a free jet and temporal flow oscillations are observed at high Reynolds numbers, in such cases. On the other hand, for low aspect ratios, asymmetric flow development occurs similar to that of duct flow in the vicinity of a sudden expansion. Thus, understanding the flow behaviour of confined jets at various aspect ratios is important for estimating its effect upon other associated phenomena, such as entrainment and mixing.

* Correspondence to: Department of Mechanical Engineering, Indian Institute of Technology, Madras 600 036, India.

Received July 1997
Revised September 1997

The stability of 2D free jets was studied experimentally by Sato [2] and Sato and Sakao [3]. Theoretical analyses for axisymmetric free jets were carried out by Batchelor and Gill [4] and Cohen and Wygnanski [5]. The bifurcation in flow solution for a two-dimensional duct with sudden expansion has been analysed theoretically by Cliffe and Greenfield [6], Sobey and Drazin [7] and Battaglia *et al.* [8]. Experimental observations for such flow configurations have been carried out by Durst *et al.* [9], Sobey [10] and Fearn *et al.* [11]. These experimental and theoretical studies have confirmed the asymmetric development of flow with respect to the midplane beyond a critical flow Reynolds number. The variation of critical Reynolds number for bifurcation with aspect ratio has been investigated in detail by Battaglia *et al.* [8]. These

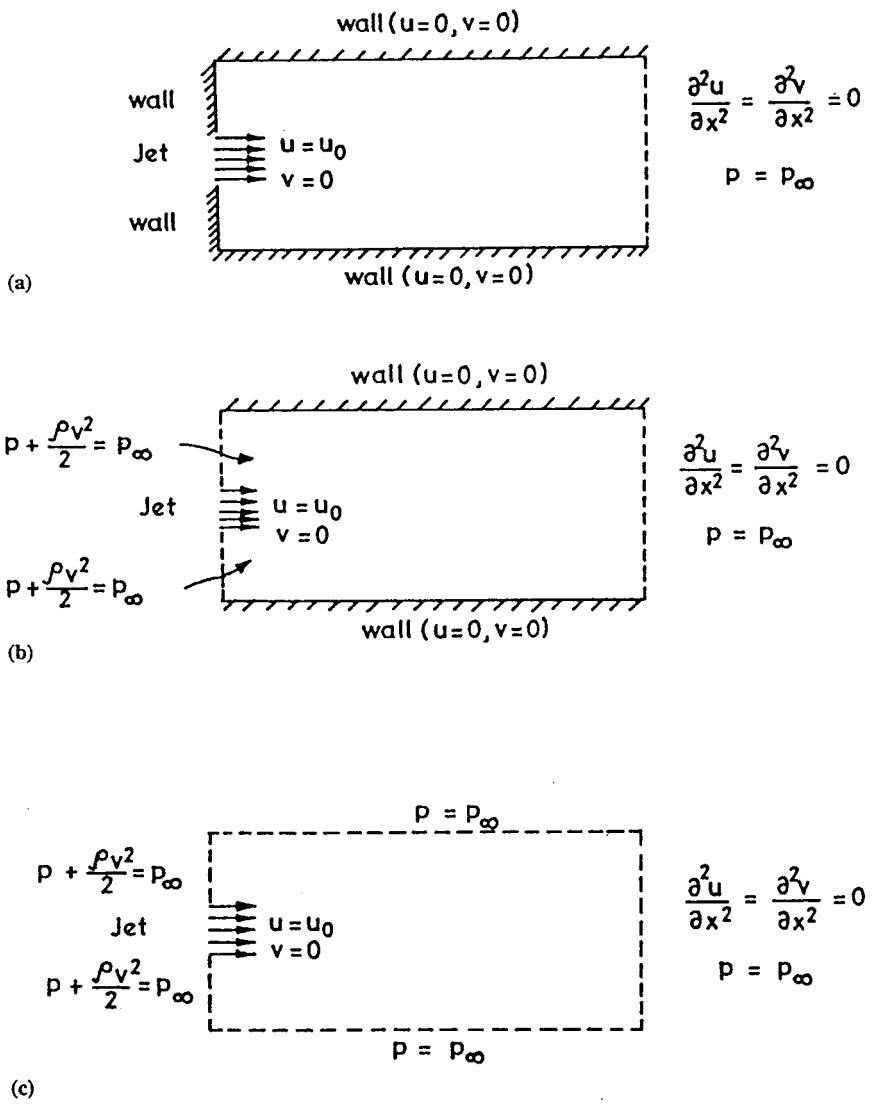

Figure 1. Geometry and boundary conditions for confined and free jets: (a) non-entraining confined jet, (b) entraining confined jet, (c) free jet.

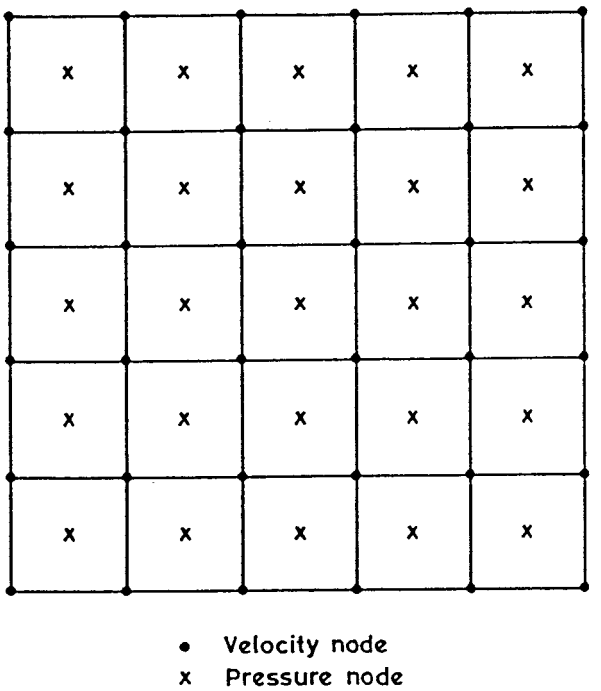

Figure 2. Staggered grid structure.

authors have also validated their numerical predictions by comparing with the experimental data of Fearn *et al.* [11].

Although many experimental studies have been conducted, the available literature on theoretical simulation of confined jet flows is some what limited. The transition of confined laminar jets from steady asymmetric flow to that of a temporally oscillating flow for larger aspect ratios, has not yet been considered. Furthermore, the case of an entraining jet located at the mouth of a duct, which occurs in several practical applications, has not been studied. In the present study, a time marching incompressible flow solver has been applied for simulating the flow features of both entraining and non-entraining jets over a wide range of aspect ratios.

2. MATHEMATICAL FORMULATION

An incompressible two-dimensional laminar jet is considered. For the sake of simplicity, the jet is assumed to be isothermal and having the same density as the ambient fluid. Also, the velocity profile at the jet inlet is taken as uniform. The dimensionless continuity and momentum equations for the 2D flow problem are given by

$$\frac{\partial u}{\partial x}+\frac{\partial v}{\partial y}=0, \tag{1}$$

$$\frac{\partial u}{\partial t}+u\frac{\partial u}{\partial x}+v\frac{\partial u}{\partial y}=-\frac{\partial p}{\partial x}+\frac{1}{Re}\left(\frac{\partial^2 u}{\partial x^2}+\frac{\partial^2 u}{\partial y^2}\right), \tag{2}$$

$$\frac{\partial v}{\partial t}+u\frac{\partial v}{\partial x}+v\frac{\partial v}{\partial y}=-\frac{\partial p}{\partial y}+\frac{1}{Re}\left(\frac{\partial^2 v}{\partial x^2}+\frac{\partial^2 v}{\partial y^2}\right), \tag{3}$$

where the variables are scaled as

$$u=\frac{\bar{u}}{u_0}, \qquad v=\frac{\bar{v}}{u_0}, \qquad p=\frac{\bar{p}}{\rho u_0^2},$$

$$x=\frac{\bar{x}}{d_j}, \qquad y=\frac{\bar{y}}{d_j}, \qquad t=\frac{\bar{t}u_0}{d_j}.$$

with the overbar indicating a dimensional variable and u_0, d_j denoting the uniform jet velocity at nozzle exit and the jet width, respectively.

The boundary conditions needed for the numerical simulation have been prescribed, depending upon the problem under consideration. For a confined jet inside a closed duct (without entrainment), the following dimensionless conditions have been enforced, as shown in Figure 1(a).

At jet inlet ($x=0$), $u=1$, $v=0$.

At the duct walls ($y=\pm y_{\max}$), $u=0$, $v=0$ due to no-slip.

No midplane symmetry has been assumed, giving allowance for asymmetric flow development beyond the critical Reynolds number.

At downstream boundary ($x=x_{\max}$), the condition of zero second-derivative has been applied for velocity components. This condition implies a linear extrapolation of the concerned flow variable at the boundary from the interior solution. Thus,

$$\frac{\partial^2 u}{\partial x^2}=\frac{\partial^2 v}{\partial x^2}=0 \quad \text{at } (x=x_{\max}).$$

The static pressure at the exit section is prescribed as the ambient pressure p_∞.

When the duct is open, entrainment is possible due to ejector action near the mouth of the jet orifice. For the entraining region, the boundary condition has been incorporated, based on the Bernoulli equation. If p_∞ is the ambient pressure, the static pressure at the inlet section outside the jet is prescribed as

$$p=p_\infty-\frac{1}{2}\rho V^2,$$

where V is the magnitude of the total flow velocity (Figure 1(b)). All the other boundary conditions are similar to those for the non-entraining case.

For comparison with available experimental work, the case of free jet flow has also been simulated. In order to simulate the free jet, the ratio between the widths of the solution domain and the jet has been taken to be very large (of the order of 250). In addition, the pressure along the side surfaces of the solution domain has also been prescribed as ambient pressure and the velocities, u, v, are extrapolated from the interior solution (Figure 1(c)), allowing for entrainment.

Subject to the above boundary conditions, the governing equations have been solved by a finite element scheme based on the projection method. Transient, as well as steady state results (if available), have been obtained for a range of Reynolds numbers in the laminar regime and for different aspect ratios (D/d_j). A brief summary of the numerical solution procedure employed in the present work is described in the next section.

3. NUMERICAL SOLUTION PROCEDURE

The Galerkin weighted residual method has been applied for formulating the discretised equations. For the sake of brevity, the discretisation procedure has been shown below, only for the x-momentum equation. Thus,

$$\iint_\Omega \dot{u} N_i \, dx \, dy = -\iint_\Omega \left(u \frac{\partial u}{\partial x} + v \frac{\partial u}{\partial y} \right) N_i \, dx \, dy - \iint_\Omega N_i \frac{\partial p}{\partial x} \, dx \, dy + \frac{1}{Re} \iint_\Omega N_i \nabla^2 u \, dx \, dy, \quad i = 1, 2, \ldots, n, \tag{4}$$

where N_i are the shape functions used for interpolation, n is the total number of velocity nodes and Ω is the solution domain. Now, integrating the viscous terms by parts to obtain the weak formulation and applying mass lumping to the transient term, the simplified form of the x-momentum equation is given by,

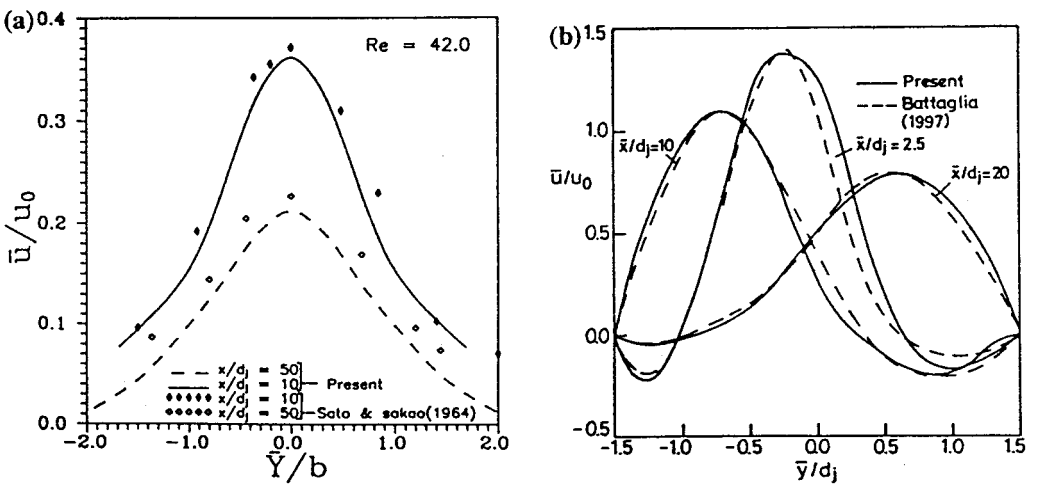

Figure 3. (a) Validation of numerical predictions with experimental data for a free jet flow; (b) validation of present predictions for confined jet flow with results in literature.

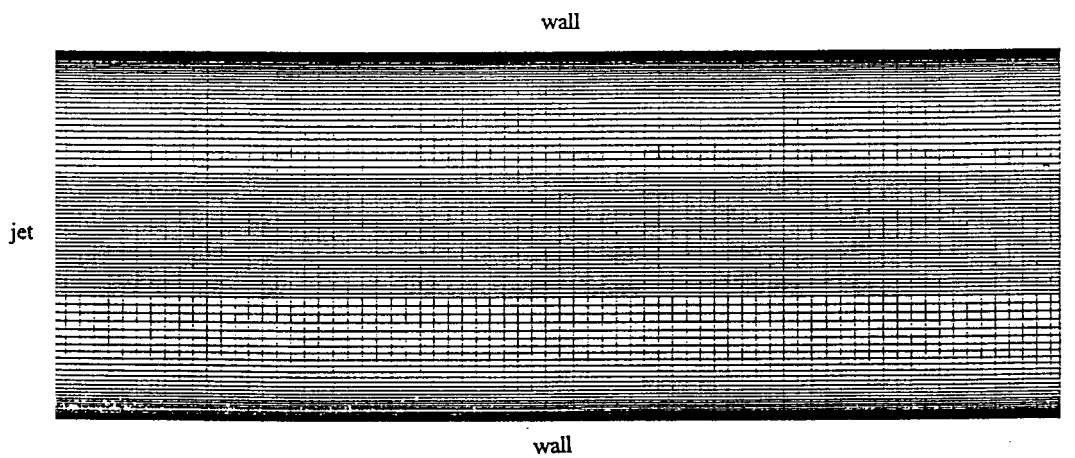

Figure 4. Typical mesh employed for computation (only 30% of total length shown).

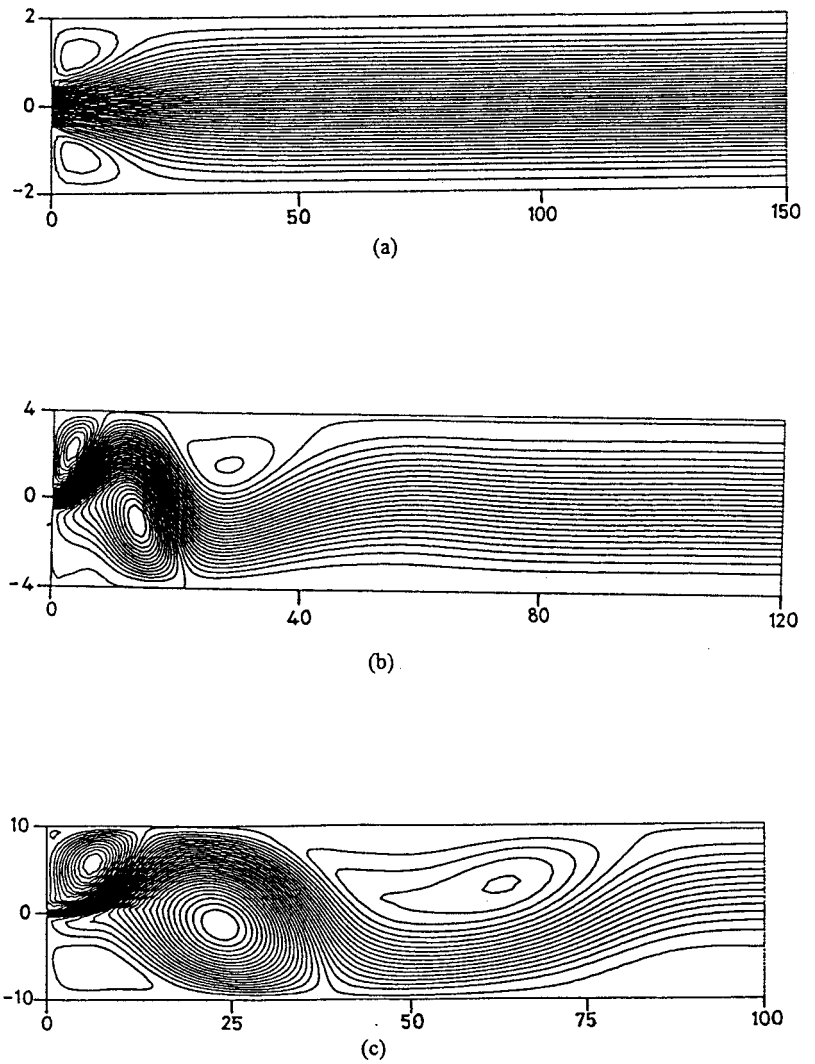

Figure 5. Effect of aspect ratio on flow structure at $Re = 100$ for non-entraining flow; (a) $AR = 4$, (b) $AR = 8$, (c) $AR = 20$.

$$\dot{u} \iint_{\Omega} N_i \, \mathrm{d}x \, \mathrm{d}y = -\iint_{\Omega} \left(u \frac{\partial u}{\partial x} + v \frac{\partial u}{\partial y} \right) N_i \, \mathrm{d}x \, \mathrm{d}y + \iint_{\Omega} N_i \frac{\partial p}{\partial x} \, \mathrm{dx} \, \mathrm{d}y - \oint N_i p n_x \, \mathrm{d}l$$
$$- \frac{1}{Re} \iint_{\Omega} \left(\frac{\partial N_i}{\partial x} \frac{\partial u}{\partial x} + \frac{\partial N_i}{\partial y} \frac{\partial u}{\partial y} \right) \mathrm{d}x \, \mathrm{d}y + \frac{1}{Re} \oint_{S} N_i \frac{\partial u}{\partial n} \, \mathrm{d}l. \tag{5}$$

For converting the above equation into matrix form, the variables u, v and p are interpolated within each element as

$$u = \sum N_j u_j, \qquad v = \sum N_j v_j, \qquad p = \sum M_j p_j, \tag{6}$$

where N_j and M_j are the shape functions used for velocity components and pressure, respectively. In the present study, four-noded quadrilateral elements have been used for velocity. The pressure is treated as a constant within each element for the momentum equations, while it is interpolated

using a bilinear form (four nodes) during the solution of continuity equation. The pressure nodes are staggered with respect to the velocity nodes (Figure 2). The final form of the finite element matrix equations corresponding to the application of x and y-momentum principles at each node are given by,

$$[M_D]\{\dot{u}_j\} = -[C]\{u_j\} - [D]\{u_j\} - [S_x]\{p_j\} \tag{7}$$

and

$$[M_D]\{\dot{v}_j\} = -[C]\{v_j\} - [D]\{v_j\} - [S_y]\{p_j\}, \tag{8}$$

where M_D, C and D are the lumped mass, convective and diffusive coefficient matrices, respectively. Also, S_x and S_y are the coefficient matrices for the pressure gradient terms.

The pressure terms in Equations (7) and (8) are handled implicitly, for updating pressure by a correction procedure similar to that in the SIMPLE family of algorithms (Mukhopadhyay *et al.* [12] and Sarma *et al.* [13]). From Equation (7), the updated u velocity after a time step of Δt is obtained as

$$[M_D]\{u_j^{n+1}\} = [M_D]\{u_j^n\} - \Delta t[C^n]\{u_j^n\} - \Delta t[D]\{u_j^n\} - \Delta t[S_x]\{p_j^{n+1}\}. \tag{9}$$

If a guess pressure field p^* is used in place of the correct pressure field p^{n+1}, then a guess velocity field u^* is obtained through the expression,

$$[M_D]\{u_j^*\} = [M_D]\{u_j^n\} - \Delta t[C^n]\{u_j^n\} - \Delta t[D]\{u_j^n\} - \Delta t[S_x]\{p_j^*\}. \tag{10}$$

Subtracting Equation (10) from Equation (9), one obtains

$$[M_D]\{u_j'\} = -\Delta t[S_x]\{p_j'\}. \tag{11}$$

Similarly, it can be shown that

$$[M_D]\{v_j'\} = -\Delta t[S_y]\{p_j'\}, \tag{12}$$

where the velocity corrections (u', v') and the pressure correction, p', are defined as

$$u' = u^{n+1} - u^*, \qquad v' = v^{n+1} - v^*, \qquad p' = p^{n+1} - p^*. \tag{13}$$

The continuity equation can now be written in matrix form as

$$\iint N_i\left(\frac{\partial u}{\partial x} + \frac{\partial v}{\partial y}\right) \mathrm{d}x\ \mathrm{d}y = [CT_x]\{u_j\} + [CT_y]\{v_j\} = 0. \tag{14}$$

It should be noted, however, that the continuity equation (14) will be satisfied exactly by the correct velocity field only, and the guess velocity field (u^*, v^*) will leave behind a mass residue. Thus, for the ith pressure node (continuity cell)

$$[CT_x]\{u_j^*\} + [CT_y]\{v_j^*\} = \{\mathrm{Res}_i\}, \tag{15}$$

and

$$[CT_x]\{u_j^{n+1}\} + [CT_y]\{v_j^{n+1}\} = 0. \tag{16}$$

Subtracting Equation (15) from Equation (16), one obtains

$$[CT_x]\{u_j'\} + [CT_y]\{v_j'\} = -\{\mathrm{Res}_i\} \quad \text{for the } i\text{th node.} \tag{17}$$

Substituting for the velocity corrections u_j' and v_j', from Equations (13) and (14), the final form of the continuity equation becomes

$$[[CT_x]\{S_x\} + [CT_y]\{S_y\}]\{p_j'\} = \frac{1}{\Delta t}[M_D]\{\mathrm{Res}_i\}. \tag{18}$$

The overall solution algorithm for the problem can now be stated as follows:

1. Assume a guess pressure field p^* and solve for the guess velocities u^* and v^* at each node using Equations (7) and (8).

2. From the guess velocities u^* and v^*, evaluate the residue (Res_i), for the continuity cell surrounding each pressure node.
3. Solve the pressure correction equation (18) to find p' at each pressure node.
4. From Equations (11) and (12), find the velocity corrections u' and v' at each node.
5. Finally, calculate the correct velocity and pressure as

$$p^{n+1} = p^* + p', \qquad u^{n+1} = u^* + u', \qquad v^{n+1} = v^* + v'.$$

The pressure correction equation was solved iteratively by the tridiagonal matrix algorithm (TDMA) with an underrelaxation factor of 0.5, and the velocities were updated iteratively within a time step Δt to provide some amount of implicitness to the velocity solutions also. The above procedure for time marching was carried out for several time steps, until a steady or oscillatory solution evolves. Convergence of the numerical solution was monitored in two different ways. The differences in the solution variable values were verified to converge within a tolerance of 10^{-4} at each node over 100 time steps. In addition, the global norm of the continuity residue, $(\Sigma\, \mathrm{Res}_i^2)^{1/2}$, was verified to converge within 10^{-3}. For some computational runs, the above convergence criteria for steady solution could not be satisfied. In such cases, the transient variation of the flow solution was obtained for a few cycles, to confirm the oscillatory nature of the flow behaviour. The typical non-dimensional time steps employed in the study were of the order of 10^{-4}.

4. VALIDATION OF THE NUMERICAL SCHEME

Since the present study is concerned with the flow structure of free and confined jets, comparisons have been made with available results in the literature for these cases. For free jet flow, the experimental results of Sato and Sakao [3], have been considered and compared with the predictions of the present scheme in Figure 3(a). The velocity profile at the jet inlet has been given as parabolic for matching with experimental conditions. It is observed that the predicted radial profiles of axial velocity agree fairly well with the experimental data at two different axial distances.

For validating the predictions for confined jet flow, comparisons with the numerical results of Battaglia *et al.* [8] have been presented in Figure 3(b) for the axial velocity profile. It is found that the agreement between the two sets of results is fairly good. A numerical mesh with 512×221 points has been employed for these predictions, with a parabolic inlet velocity profile, as in the study of Battaglia *et al.* [8]. For a given ratio of duct-to-jet width, the predicted critical Reynolds number value for bifurcation of flow solution was found to be slightly different from the value obtained by the above authors. For instance, the axial velocity profile predictions here at a Reynolds number of 190 agree with those reported by Battaglia *et al.* [8] for a Reynolds number of 187. But for this difference in Reynolds number, the flow features of asymmetric jet development inside the duct were found to be virtually identical. The minor deviations in the results of the present study and those of the earlier investigations can be attributed to the differences in the numerical scheme and the round-off/discretisation errors.

To illustrate the grid-independence of the predicted results, grids with 111×111, 256×111 and 512×221 points have been considered for simulating duct flow in the vicinity of a sudden expansion with $AR = 3.0$ and $Re = 190$. It was observed that the velocity profiles at non-dimensional axial distances of $x/d = 2.5$, 10 and 20, exhibit a maximum deviation of the order

of 0.5% for the above grids, indicating the grid-independence of the results. For all the numerical predictions of the present study, meshes with 10000–100000 grid points have been employed. A typical mesh employed for the simulation is shown in Figure 4, for about 30% of the total length considered for computation.

5. RESULTS AND DISCUSSIONS

Flow results have been predicted for a range of aspect ratios and Reynolds numbers in the laminar flow regime, for both entraining and non-entraining cases. The range of parameters has been selected so as to illustrate the symmetric/asymmetric jet development in steady state or the transient jet flow structure in the presence of confining walls.

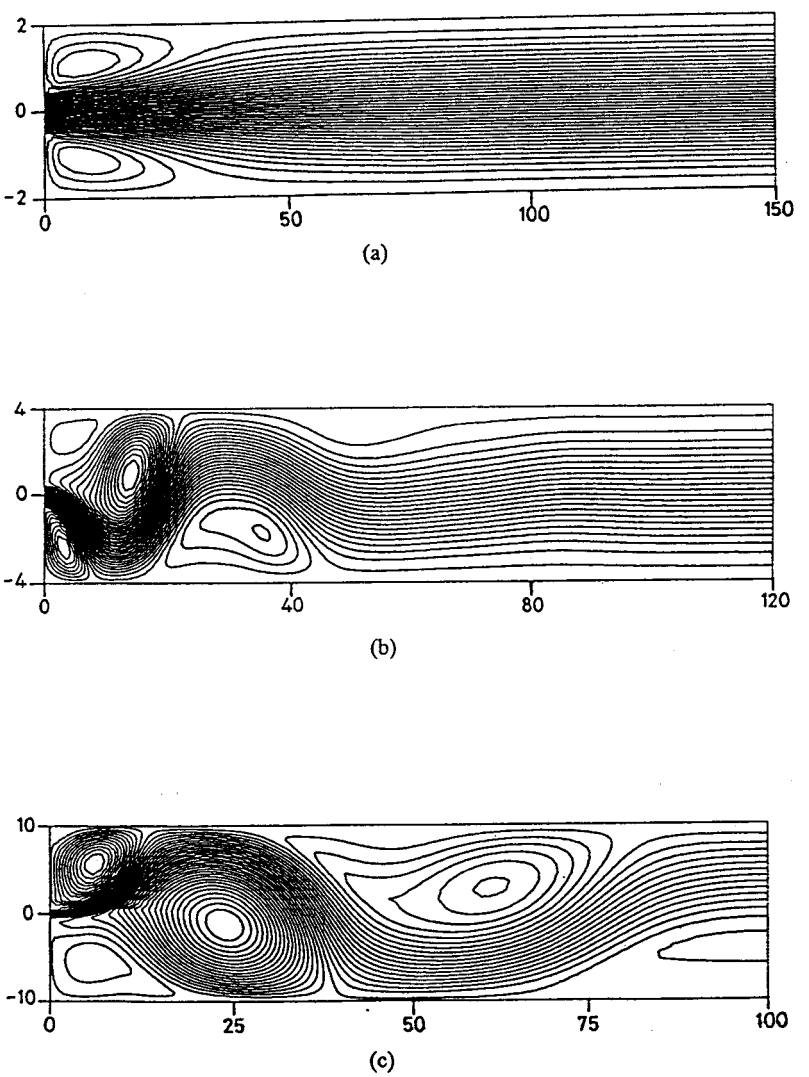

Figure 6. Effect of aspect ratio on flow structure at $Re = 200$ for non-entraining flow; (a) $AR = 4$, (b) $AR = 8$, (c) $AR = 20$.

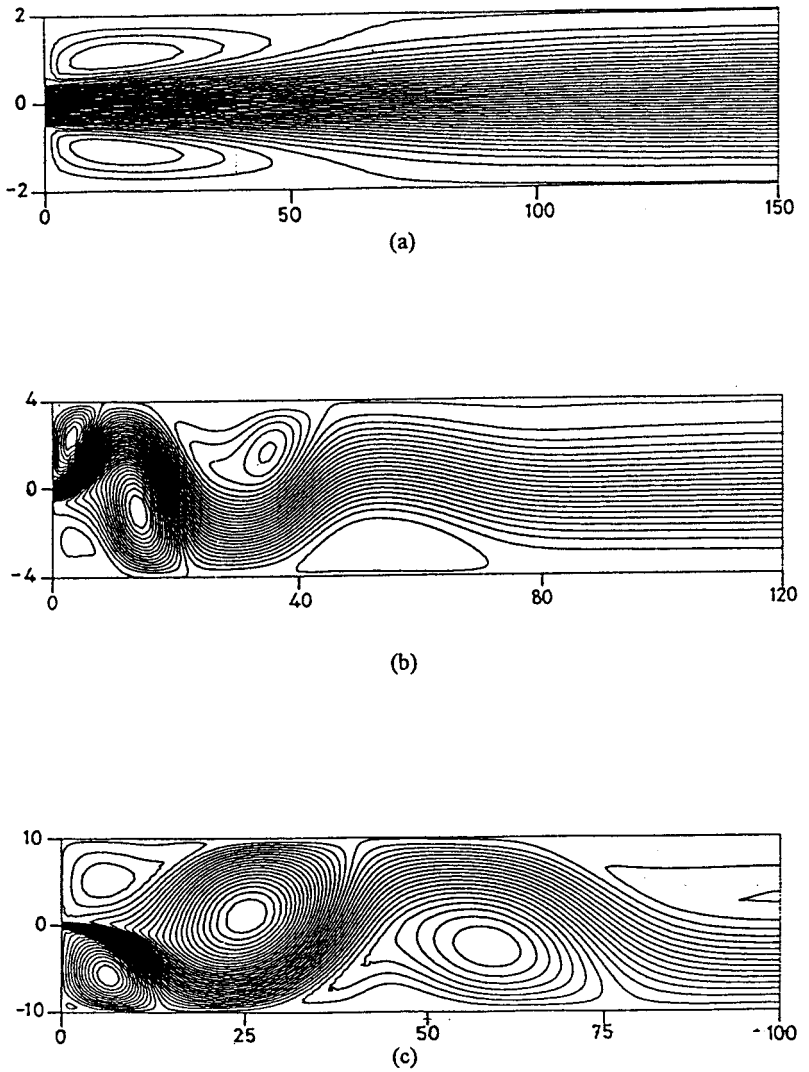

Figure 7. Effect of aspect ratio on flow structure at $Re = 400$ for non-entraining flow; (a) $AR = 4$, (b) $AR = 8$, (c) $AR = 20$.

5.1. Streamline patterns

In Figures 5–7, the steady state streamline patterns at different Reynolds numbers and aspect ratios are depicted for the non-entraining flow situation. In Figure 5(a)–(c), the influence of aspect ratio on flow structure at $Re = 100$ is shown. It is observed that for a low aspect ratio such as $AR = 4$, the jet development is symmetric and counter-rotating vortices are seen immediately after the sudden expansion. The jet decay is rapid and the transition from jet-to-duct flow occurs in a short distance. At a higher aspect ratio of $AR = 8$ (Figure 5(b)), it is observed that the steady state jet flow development is asymmetric. Also, the transition from jet-to-duct flow occurs over a longer distance. For a still higher aspect ratio of 20 (Figure 5(c)), it is seen that asymmetric flow exhibits a wavy pattern with a larger wavelength and the flow

development inside the duct occurs over a larger axial distance. A point to be noted here is that the asymmetry in the flow pattern corresponds to a bimodal steady configuration with the jet turning upwards or downwards in a random manner, during any computational run.

In Figure 6(a)–(c), the flow patterns at $Re = 200$ are shown for different aspect ratios. Similar figures for $Re = 400$ are shown in Figure 7(a)–(c). It is observed from these figures that for symmetric jet flow at low aspect ratios ($AR = 4$), the length of the recirculating eddy increases with jet Reynolds number. In turn, jet decay and transition to duct flow occurs over larger axial distances at higher Reynolds number values. In other words, the spread angle of the jet inside the duct decreases with Reynolds number, as expected. However, for larger aspect ratios ($AR = 8$ and 20), the asymmetric flow development is influenced mainly by the aspect ratio and not significantly by the Reynolds number. Thus, for any given aspect ratio, the patterns are almost identical for all the Reynolds numbers considered in the present study,

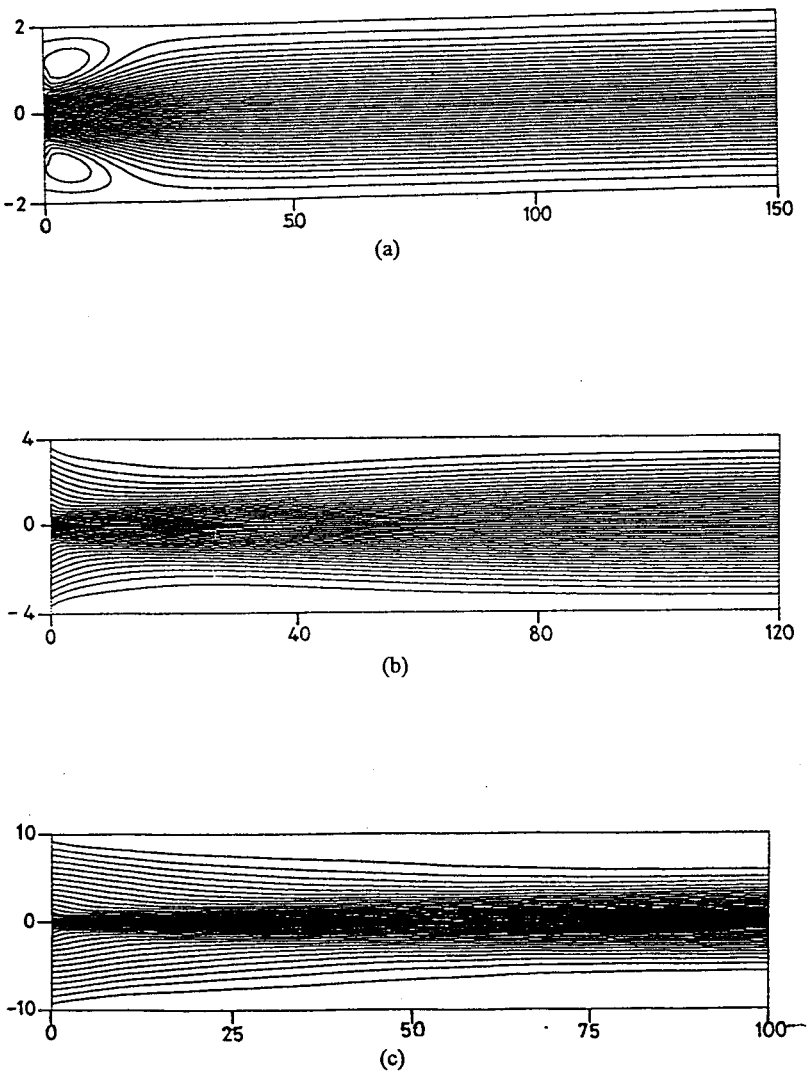

Figure 8. Effect of aspect ratio on flow structure at $Re = 100$ for entraining flow; (a) $AR = 4$, (b) $AR = 8$, (c) $AR = 20$.

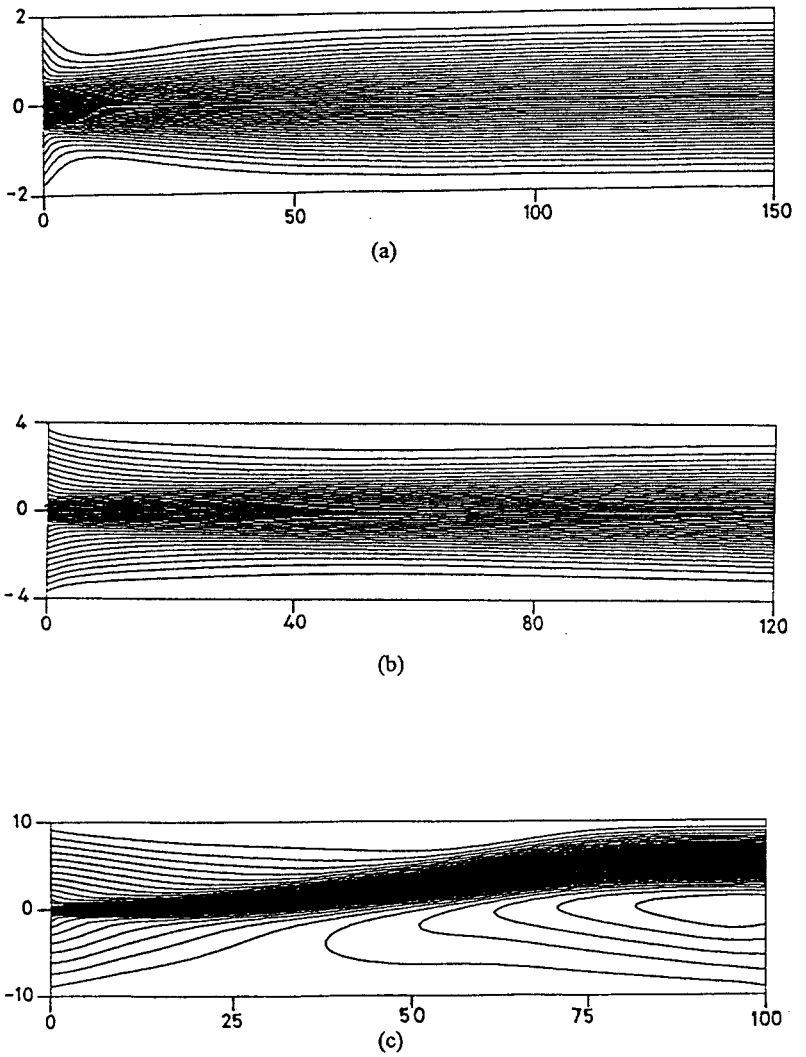

Figure 9. Effect of aspect ratio on flow structure at $Re = 200$ for entraining flow; (a) $AR = 4$, (b) $AR = 8$, (c) $AR = 20$.

except that the flow development in one case may appear as a mirror image of another (see Figure 5(c), Figure 6(c) and Figure 7(c)). This is in view of the fact that the jet flow development has equal probability of existing in any one of the bimodal states for these asymmetric cases.

The flow patterns for the entraining case are shown in Figures 8 and 9, for the Reynolds numbers of 100 and 200, respectively. At a low Reynolds number and low aspect ratio (Figure 8(a)), it is observed that recirculating eddies exist at the mouth of the duct, even in the presence of entrainment. The jet decay and transition to duct flow are seen to occur over a short distance, as in the case of non-entraining jet flow. The flow development appears to be symmetric and the jet exhibits more stability. These trends can be attributed to the following factors. The asymmetric flow development of a non-entraining jet occurs due to the convective instability of the shear layers at jet periphery. When entrainment is present, momentum is

shared between the jet shear layer and the ambient fluid, which tends to increase the jet stability. Therefore, jet development is seen to be symmetric even at larger aspect ratios (Figure 8(b) and (c)), when entrainment is allowed at the mouth of the duct. Another feature that is apparent from Figure 8(a)–(c) is that the jet decay is slower for a higher aspect ratio; this illustrates that the higher magnitudes of viscous stresses at lower aspect ratios are responsible for more rapid decay. In Figure 9(a)–(c), the flow patterns at different aspect ratios are shown for $Re = 200$. At a low aspect ratio ($AR = 4$), a nearly stagnant zone is seen near the mouth of the duct and the recirculatory eddies observed at the duct inlet for $Re = 100$ (Figure 8(a)) are not present. For $Re = 200$ and $AR = 20$, it is observed that jet development becomes asymmetric even in the presence of entrainment. The wavelength of asymmetric spatial oscillations is higher than those observed for the non-entraining cases.

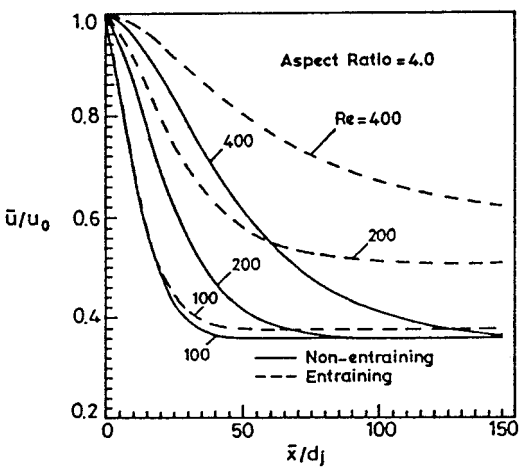

Figure 10. Variation of axial velocity along the centreline at low aspect ratio.

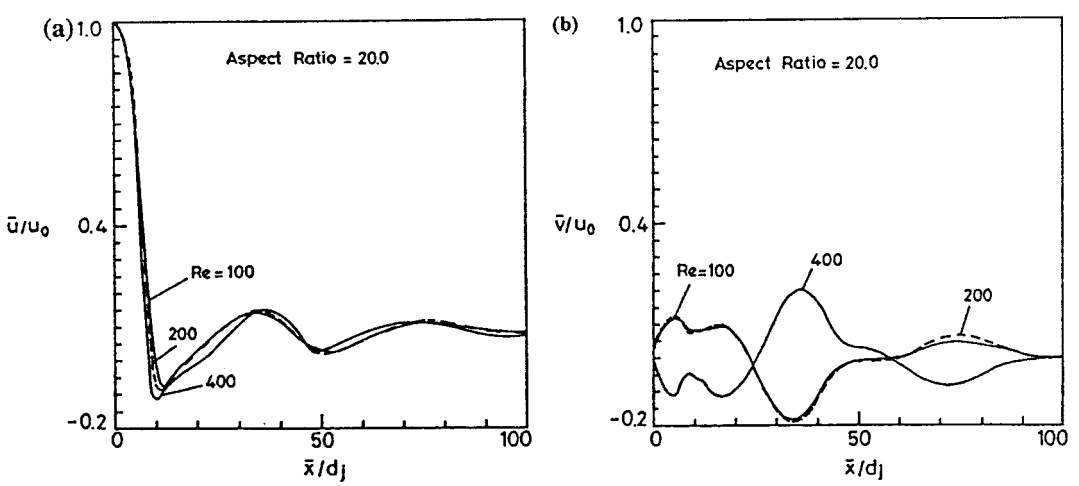

Figure 11. (a) Variation of axial velocity with distance at high aspect ratio; (b) variation of transverse velocity with distance at high aspect ratio.

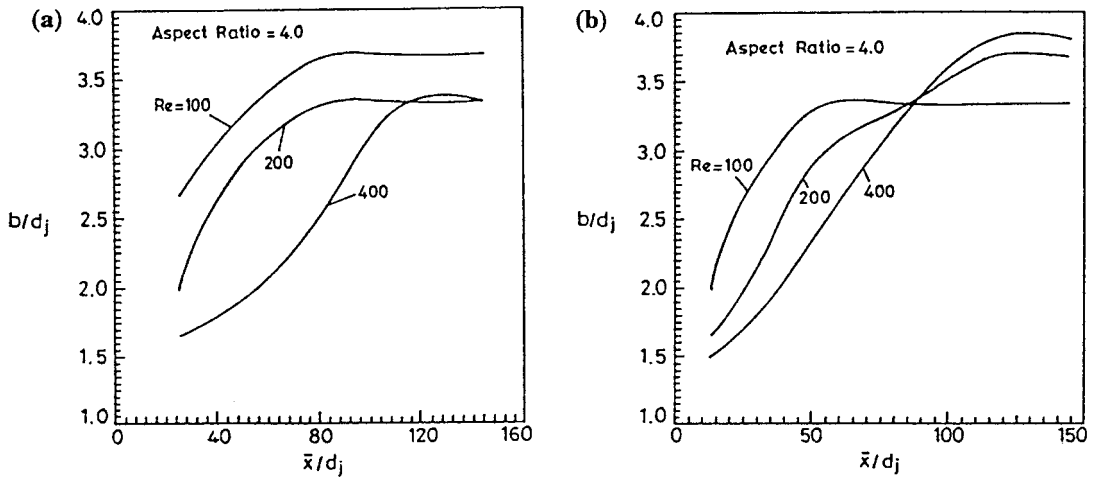

Figure 12. (a) Jet spread for non-entraining flow; (b) Jet spread for entraining flow.

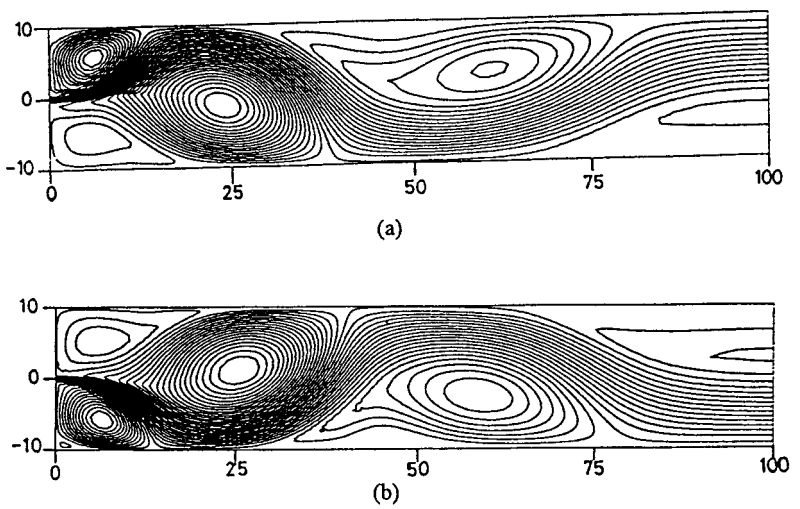

Figure 13. Evolution of flow structure with time for non-entraining flow at $Re = 500$ and $AR = 20$: (a) $t = 1.25$, (b) $t = 1.81$.

5.2. Velocity decay

The axial variations of u-velocity are plotted in Figure 10 for the entraining and the non-entraining flow situations, at an aspect ratio of 4. These plots illustrate that the jet decay is slower at a higher Reynolds number. The decay patterns are similar for the cases with and without entrainment. However, the velocity values are larger in magnitude when entrainment is present, as expected. The variations of both u- and v-velocity components along the centre line are shown in Figure 11(a) and (b) for the Reynolds numbers of 100, 200 and 400, at an aspect ratio of 20. The wavy patterns corresponding to the asymmetric flow development are observed for all the three Reynolds numbers. While the u-velocity variation is almost identical for all the three cases, the v-velocity profiles appear as mirror images depending on whether the jet tilts towards the upper or lower wall of the duct. These results corroborate the earlier

conclusions that the asymmetric flow pattern is not significantly affected by the Reynolds number at a given aspect ratio.

In Figure 12(a) and (b), the dimensionless half jet width has been plotted against the dimensionless axial distance for different Reynolds numbers. Here, the jet half width is defined as the distance where the u-velocity reaches 50% of its value on the axis. It is observed that at low Reynolds numbers, the jet width becomes a constant at a shorter distance, implying a more rapid decay. This feature is observed for both entraining and non-entraining cases. It is also seen that an entraining jet at low Reynolds number decays very rapidly due to momentum sharing between the jet and the entrained fluid.

In Figure 13(a) and (b), the variations in jet flow pattern with respect to time for large aspect ratio ($AR = 20$) and Reynolds number ($Re = 500$) are shown. It is evident that the jet exhibits temporal oscillations when the Reynolds number is very high for a large aspect ratio. Indeed, similar features are observed at the aspect ratio of 20 and Reynolds number of 600, for the entraining jet flow (Figure 14(a) and (b)) Unlike in the earlier cases discussed, these flow solutions do not converge to a steady state and the jet keeps oscillating with respect to time as shown in the figures. Occurrence of such temporal oscillations have been observed for two-dimensional free jets (Fearn *et al.* [11]) as well.

The critical Reynolds numbers for the onset of asymmetry and temporal oscillations have been plotted for different aspect ratios in Figure 15(a) and (b) for the non-entraining and entraining jet situations. It is evident that transient fluctuations start at a Reynolds number higher than the critical Reynolds number limit for the asymmetry, at a given aspect ratio. It is also observed that with entrainment, the Reynolds number limits for both forms of instabilities are higher. It may, therefore, be surmised that entrainment causes jet flow to become more stable, since momentum exchange occurs between the shear layer of jet and the entrained fluid.

In Figure 16, the variations in mass entrainment per unit width for a 2 mm jet placed at the mouth of a duct are shown for various aspect ratios and Reynolds numbers. At lower aspect ratios, entrainment increases with Reynolds number almost at a linear rate. However, for a higher aspect ratio ($AR = 20$), the increase in entrainment with Reynolds number is affected

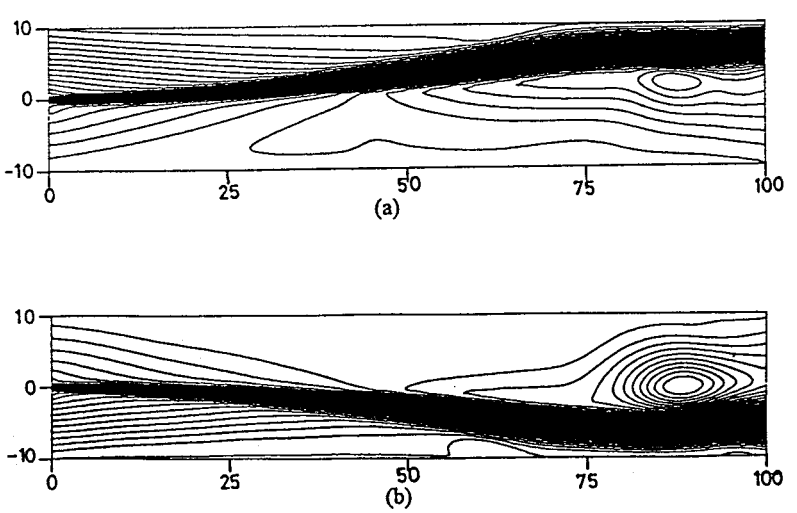

Figure 14. Evolution of flow structure with time for entraining flow at $Re = 600$ and $AR = 20$: (a) $t = 1.25$, (b) $t = 210$.

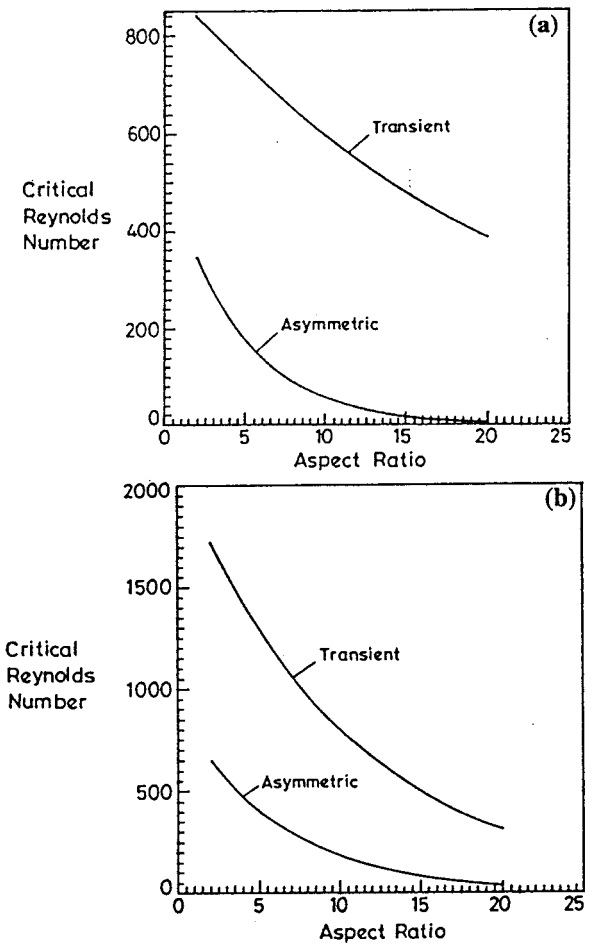

Figure 15. (a) Critical Reynolds number variation for non-entraining flow; (b) Critical Reynolds number variation for entraining flow.

considerably by the occurrence of asymmetric flow development. This feature is also evident in Figure 14, since the major part of entrainment is seen to occur only on the side towards which the jet swings. On the other side, a large recirculatory eddy is observed, which may also contribute to reduction in entrainment by blocking part of the flow area. For very high Reynolds numbers, the entrainment also becomes unsteady and acquires a periodically varying trend. Therefore, the steady mass flow rate through the duct has not been plotted in Figure 16 for high *Re*.

6. SUMMARY

A theoretical formulation has been developed for analysing two-dimensional entraining and non-entraining laminar jet flows inside ducts. The predicted results have been validated with available experimental and theoretical data for free and confined jets. It is observed that at a fixed aspect ratio, when jet Reynolds number is increased, the flow development first becomes

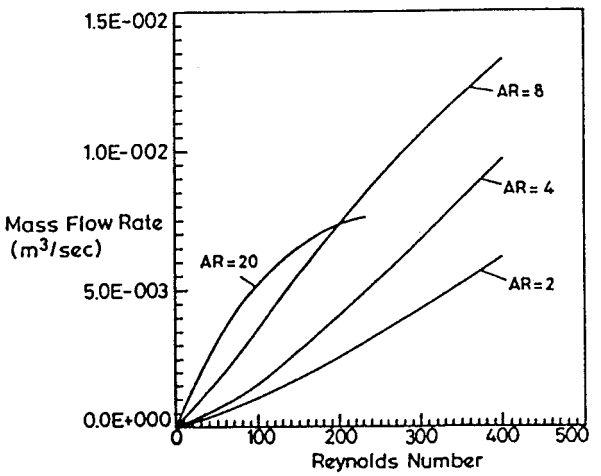

Figure 16. Effect of aspect ratio on the level of entrainment.

asymmetric, and for still higher Reynolds numbers, it becomes temporally oscillatory. The level of entrainment of ambient fluid is severely affected by such instabilities.

APPENDIX A. NOMENCLATURE

AR	aspect ratio
b	jet half width
D	duct width
d_j	jet width at the mouth of the inlet
N	shape function
$\bar{p}$	static pressure
p_∞	ambient pressure
p	non-dimensional pressure
Re	Reynolds number based on jet width and inlet velocity
t	non-dimensional time
$\bar{t}$	time
u_0	x-component of velocity at the jet inlet
u	non-dimensional x-component of velocity
$\bar{u}$	x-component of velocity
v	non-dimensional y-component of velocity
$\bar{v}$	y-component of velocity
V	flow speed ($V^2 = u^2 + v^2$)
x	non-dimensional axial distance
$\bar{x}$	axial distance
$x_{\max}$	axial distance of the outlet boundary for the solution domain
y	non-dimensional lateral distance
$\bar{y}$	lateral distance
$y_{\max}$	maximum lateral distance from mid plane ($y_{\max} = D/2.0$)

Greek symbols

ρ	non-dimensional density
$\bar{\rho}$	density

REFERENCES

1. Schlichting H. *Boundary Layer Theory* (7th edn). McGraw-Hill: New York, 1979.
2. Sato H. The stability and transition of a two-dimensional jet. *Journal of Fluid Mechanics* 1960; **7**: 53–80.
3. Sato H, Sakao F. An experimental investigation of the instability of a two-dimensional jet at low Reynolds numbers. *Journal of Fluid Mechanics* 1964; **20**: 337–352.
4. Batchelor GK, Gill AE. Analysis of the stability of axisymmetric jets. *Journal of Fluid Mechanics* 1962; **14**: 529–551.
5. Cohen J, Wygnanski I. The evolution of instabilities in the axisymmetric jet. Part 1. The linear growth of disturbances near the nozzle. *Journal of Fluid Mechanics* 1987; **176**: 191–219.
6. Cliffe KA, Greenfield AC. Some comments on laminar flow in symmetric two-dimensional channels. Harwell Report AERE-TP, 1982; 939.
7. Sobey IJ, Drazin PG. Bifurcations of two-dimensional channel flows. *Journal of Fluid Mechanics* 1986; **171**: 263.
8. Battaglia F, Tavener SJ, Kulkarni AK, Merkle CL. Bifurcation of low Reynolds number flows in symmetric channels. *AIAA Journal* 1997; **35**: 99–105.
9. Durst F, Melling A, Whitelaw JH. Low Reynolds number flow over a plane symmetrical sudden expansion. *Journal of Fluid Mechanics* 1974; **64**: 111.
10. Sobey IJ. Observation of waves during oscillatory channel flow. *Journal of Fluid Mechanics* 1985; **151**: 395.
11. Fearn RM, Mullin T, Cliffe KA. Non-linear flow phenomena in a symmetric sudden expansion. *Journal of Fluid Mechanics* 1990; **211**: 595–608.
12. Mukhopadhyay A, Sundararajan T, Biswas G. An explicit transient algorithm for predicting incompressible viscous flows in arbitrary geometry. *International Journal of Numerical Methods in Fluids* 1993; **17**: 975–993.
13. Sarma ASR, Shenoy AK, Sundararajan T, Shet USP, Ramjee V. Finite element simulation of 2D incompressible laminar jet flows. In *Proceedings of the 22nd FMFP National Conference*, 1995; 387–393.

